Materials Characterization 149 (2019) 133–142

Contents lists available at ScienceDirect

Materials Characterization

journal homepage: www.elsevier.com/locate/matchar

Microstructure of hard biocompatible $Ti_{1-x}Au_x$ alloys

Yan Xin[a,*], Ke Han[a], Eteri Svanidze[b,1], Tiglet Besara[c], Theo Siegrist[a,e], Emilia Morosan[b,d,**]

[a] National High Magnetic Field Laboratory, Florida State University, Tallahassee, FL 32310, USA
[b] Department of Physics and Astronomy, Rice University, Houston, TX 77005, USA
[c] Department of Physics, Astronomy and Materials Science, Missouri State University, Springfield, MO 65897, USA
[d] Materials Science and NanoEngineering, Rice University, Houston, TX 77005, USA
[e] Department of Chemical and Biomedical Engineering, FAMU-FSU College of Engineering, Tallahassee, FL 32310, USA

ARTICLE INFO

Keywords:
Ti—Au alloys
Hardness
Microstructures
TEM

ABSTRACT

$Ti_{1-x}Au_x$ binary alloys are biocompatible materials. We studied the hardness and the microstructures of six casted $Ti_{1-x}Au_x$ alloys with Au molar fraction x = 0.22, 0.25, 0.335, 0.5, 0.6 and 0.8 by transmission electron microscopy down to atomic level. $Ti_{1-x}Au_x$ alloys with *x* from 0.2 to 0.40 have high hardness, in which the β-Ti_3Au is the dominating phase. This reveals that intermetallic β-Ti_3Au is the hardest of all intermetallic $Ti_{1-x}Au_x$ alloys. Alloys with *x* from 0.4 to 0.8 are softer, and their hardness is similar to that of casted pure Ti. Very high density nanotwins are observed in phases, such as fcc Ti, β-TiAu, $TiAu_2$, and Au(Ti). An interesting checker board pattern of defects consisting of orthogonal three dimensional bands of extremely high density nanotwins with a width of 2 to 3 {111} atomic planes is observed in Au(Ti). The high density defects may explain the relatively high hardness comparable to pure casted Ti for samples with high Au content. The hard β-Ti_3Au or the nanotwinned Au might be a promising candidate for hard coating.

1. Introduction

Ti-rich or Au-rich alloys are biomedical compatible alloys and have wide biomedical usages, such as in dentistry, implant or part replacements [1,2]. One of the important properties for material applications is the material hardness, which affects the lifetime of an artificial part or device. For the dental applications, it has been reported that $Ti_{1-x}Au_x$ alloy hardness ranges from 1.7 to 4.1 GPa for a low Au content with Au of 2 to 12 at.% [3,4], and for dental restorative materials, the titanium alloy has a Vickers hardness value of 3.49 GPa and the gold alloy of 1.35 GPa [5]. For a given Ti—Au composition, the equilibrium intermetallic compounds that form from the melt can be deduced from the Ti—Au phase diagram, which has been experimentally determined in 1983 by J. L. Murray [6]. Later, this system has been reassessed using thermodynamic calculations via the CALPHAD technique, and a general agreement was obtained between experimental and calculated phase diagrams. However, some details are still uncertain, such as the solidus of β-Ti and transformations between TiAu allotropes [7].

Table 1 lists all known $Ti_{1-x}Au_x$ phases. The high- and low-temperature equilibrium solid phases of Ti are β-Ti (bcc, space group *Im*-3*m*, #229) and α-Ti (hcp, space group $P6_3/mmc$, #194) respectively. They correspond to Au solubility of 15 at.% and 1.7 at.%, respectively [6]. The metastable fcc Ti phase has been identified in thin films, in a fine-grained TiMoFe alloy, at interfaces, or induced by severe plastic deformation [8,9]. The fcc Ti phase usually has grain sizes < 0.5 μm. When the Au content increases to 25 at.% Au, Ti_3Au can form. There are two different crystal structures of Ti_3Au: α-Ti_3Au (Cu_3Au structure type, space group Pm-3 m, #221) and β-Ti_3Au (Cr_3Si structure type, space group *Pm*-3*n*, #223) [10]. When the Au content increases to 50 at.%, the equiatomic TiAu compound forms. The TiAu allotropic forms are α-TiAu (CuTi structure type, space group P4/nmm O2, #129), β-TiAu (AuCd B19 structure type, space group *Pmma*, #51) and γ-TiAu (CsCl B2 structure type, space group *Pm*-3*m*, #221) [6]. TiAu is a shape-effect alloy that shows a martensitic transformation from γ-TiAu to β-TiAu [11,12]. Mechanical properties of the alloys with low Au (x < 15 at.%) content have been reported to be enhanced due to solid-solution strengthening of α-Ti, but the phases become brittle for $Ti_{0.85}Au_{0.15}$ when Ti_3Au precipitate extensively at grain boundaries [3]. Recently the hardness and coefficient of friction of β-Ti_3Au has been studied [13].

The previous microstructure studies of $Ti_{1-x}Au_x$ alloys were mostly focused on $x = 0.5$ for its application as a shape-memory alloy. It is

* Corresponding author.
** Correspondence to: E. Morosan, Department of Physics and Astronomy, Rice University, Houston, TX 77005, USA.
E-mail addresses: xin@magnet.fsu.edu (Y. Xin), emorosan@rice.edu (E. Morosan).
[1] Current address: Max-Planck-Institut für Chemische Physik fester Stoffe, Nöthnitzer Straße 40, 01187 Dresden, Germany.

https://doi.org/10.1016/j.matchar.2019.01.013
Received 3 December 2018; Received in revised form 16 January 2019; Accepted 18 January 2019
Available online 19 January 2019
1044-5803/ Published by Elsevier Inc.

Table 1
A list of possible Ti−Au phases.

Alloy	Allotrope	Space group	Lattice parameter
Ti	α (hcp)	$P6_3/mmc$ (194)	a = 0.2954, b = 0.2954, c = 0.4682 nm, α = 90, β = 90, γ = 120°
	β (bcc)	$Im\text{-}3m$ (229)	a = 0.3327, b = 0.3327, c = 0.3327 nm, α = 90, β = 90, γ = 90°
	γ (fcc)	Fm-3m	a = 0.431 nm
Ti_3Au	α (Cu_3Au structure)	$Pm\text{-}3m$ (221)	a = 0.4096, b = 0.4096, c = 0.4096 nm, α = 90, β = 90, γ = 90°
	β (Cr_3Si structure)	$Pm\text{-}3n$ (223)	a = 0.50889, b = 0.50889, c = 0.50889 nm, α = 90, β = 90, γ = 90°
Ti_2Au		$I4/mmm$ (139)	a = 0.3430, b = 0.3430, c = 0.8538 nm, α = 90, β = 90, γ = 90°
TiAu	α	$P4/nmm$ O2 (129)	a = 0.3335, b = 0.3335, c = 0.6028 nm, α = 90, β = 90, γ = 90°
	β	$Pmma$ (51)	a = 0.460, b = 0.293, c = 0.485 nm, α = 90, β = 90, γ = 90°
	γ	$Pm\text{-}3m$ (221)	a = 0.3254, b = 0.3254, c = 0.3254 nm, α = 90, β = 90, γ = 90°
$TiAu_4$		$I4/m$ (87)	a = 0.6485, b = 0.6485, c = 0.4002 nm, α = 90, β = 90, γ = 90°

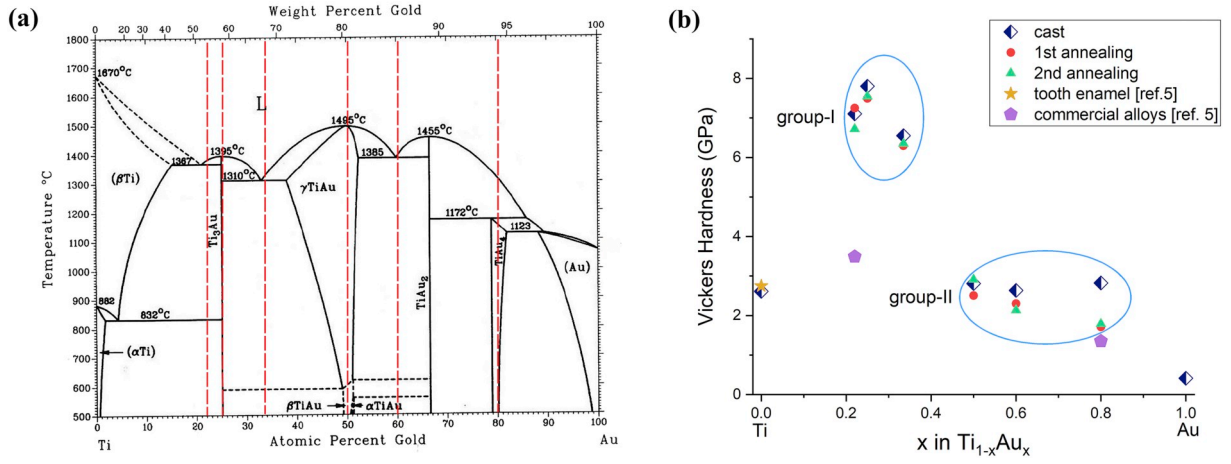

Fig. 1. (a) The six studied $Ti_{1-x}Au_x$ alloys (x = 0.22, 0.25, 0.335, 0.5, 0.6 and 0.8) indicated by dashed lines on the phase diagram by J. L. Murray [2]. (b) A plot summarizes the HV hardness values for all the alloys. Reference points from ref. [5] are added.

Table 2
Experimental measured Vickers hardness (GPa) of cast and annealed $Ti_{1-x}Au_x$ alloys.

Alloys	Au content (x)	Cast	1st annealing	2nd annealing
Ti	0	2.61 ± 0.21		
Ti0.78Au0.22	0.22	7.10 ± 0.11	7.25 ± 0.10	6.72 ± 0.33
Ti0.75Au0.25	0.25	7.80 ± 0.20	7.49 ± 0.08	7.54 ± 0.17
Ti0.665Au0.335	0.335	6.55 ± 0.20	6.29 ± 0.29	6.35 ± 0.11
Ti0.5Au0.5	0.5	2.81 ± 0.09	2.51 ± 0.09	2.91 ± 0.17
Ti0.4Au0.6	0.6	2.64 ± 0.23	2.30 ± 0.15	2.13 ± 0.36
Ti0.2Au0.8	0.8	2.83 ± 0.08	1.71 ± 0.07	1.79 ± 0.05
Au	1	0.41 ± 0.04		

common to have twins in fcc structured $Ti_{1-x}Au_x$ alloys. Most of twins are {111} type I twins, and the crystallographic information on twin structures and habit planes have been studied in TiAu [14]. In this paper, we report a comprehensive transmission electron microscopy (TEM) study of the microstructures of six cast alloys of different compositions across the whole Au composition range to obtain a better understanding of the hardness behavior of $Ti_{1-x}Au_x$ alloys.

2. Experimental Procedure

$Ti_{1-x}Au_x$ alloy were prepared by arc melting Ti (Cerac, 99.99%) and Au (Cerac, 99.99%) in different proportions. The mass losses after the arc melting process are < 0.3 at.%. To ensure homogeneity, the samples were re-melted several times, then fast cooled to form buttons of about 5 mm diameter. Two types of sample annealing were carried out. The first annealing procedure consisted of ramping the samples to 900 °C and holding at this temperature for 7 days. The second annealing was carried out in reference to the melting temperature: the samples were heated at 0.5Tm (Tm: melting temperature) for 1 h and then annealed at 0.3Tm for 8 h, with Tm taken from the Ti−Au binary phase diagram. Bulk samples were prepared for microhardness test and scanning electron microscopy (SEM) imaging. The button samples were hot-press mounted in a conducting bakelite puck of 2 cm diameter, and then grinded on SiC paper to have a flat surface. Final polishing was done using 0.04 μm colloidal silica suspension in a Buehler vibratory polisher overnight. Sample surface was finally cleaned with DI water.

X-ray diffraction (XRD) data were collected at room temperature from the polished bulk specimens, using a custom four-circle Huber diffractometer integrated with a Rigaku HR3 rotating anode source providing monochromated Cu Kα radiation.

Vickers Hardness (HV) was measured in a Tukon 2100 microhardness tester, equipped with a Vickers diamond pyramid indenter. Tests were conducted using a 300 g load and a duration of 10 s. SEM images were obtained at 15 keV and a working distance of 5 mm in a Zeiss 1540EsB SEM.

Samples with compositions of x = 0.22, 0.25, 0.335, 0.5, 0.6 and 0.8 were selected for this study. The compositions of these selected samples are indicated as dashed lines in the Ti−Au binary phase diagram [6] (Fig. 1a). TEM samples were prepared by conventional grinding using SiC paper down to < 20 μm thick. Then thinned sample piece was mounted on a Cu TEM grid for extra support before being ion

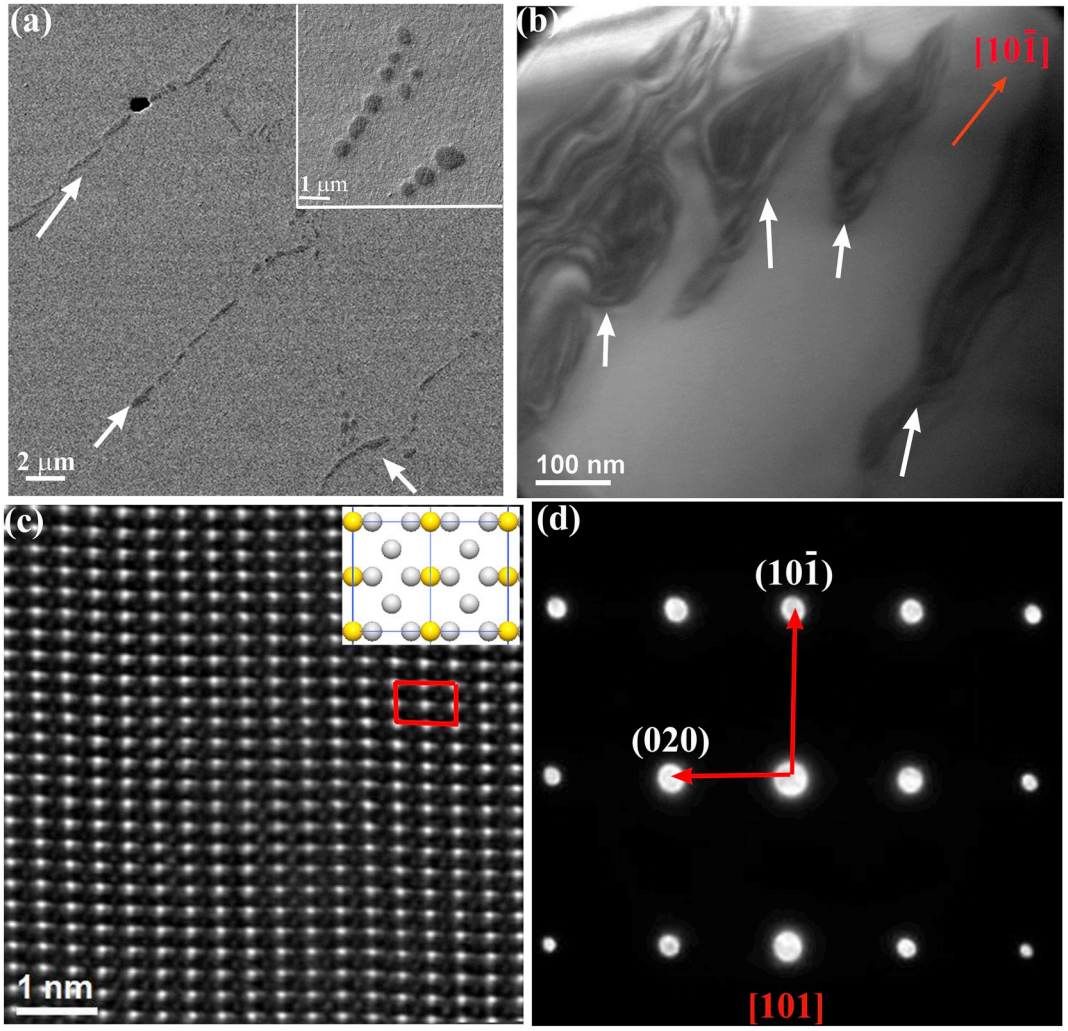

Fig. 2. (a) An SEM image of $Ti_{0.75}Au_{0.25}$ with second phase α-Ti_3Au indicated by arrows; inset: enlarged view of the second phase. (b) BF-TEM image of the major phase β-Ti_3Au, showing no defects; the dark lines/bands are diffraction contours, typical contrast from perfect crystals. (c) Atomic resolution HAADF-STEM *Z*-contrast image along [101] β-Ti_3Au; inset: projected unit cell; Au: yellow; Ti: grey. (d) Diffraction pattern of β-Ti_3Au along [101]. (For interpretation of the references to color in this figure legend, the reader is referred to the web version of this article.)

milled. Gatan PIPS was used for final thinning using the milling condition of 5 kV at an angle of 6°.

TEM observations were carried out using a JEOL probe-aberration-corrected cold field emission JEM-ARM200cF microscope operating at 200 kV. TEM images and electron diffraction patterns were recorded with a Gatan Orius CCD camera with an acquisition time of 1 s. The high-angle-annular-dark-field scanning transmission electron microscopy (HAADF-STEM) imaging was acquired on a JEOL HAADF detector using a probe size of 0.078 nm and a camera length of 8 cm. The probe convergence angle is 21 mrad and the HAADF collection angle is 68 mrad.

3. Results

Materials hardness usually has a direct relationship to mechanical properties, such as strength and ductility [15]. Measuring hardness is a rapid, convenient, and inexpensive way to obtain information on the overall mechanical strength of a material, particularly for small samples. The results of micro-hardness tests performed on the $Ti_{1-x}Au_x$ alloys are summarized in Fig. 1b, and the measured hardness values with experimental standard deviation are listed in Table 2 for each alloy. The alloys can be divided into two groups according to their hardness values: group-I with $x < 0.4$, has higher hardness values (6.55–7.80 GPa), and group-II with $x > 0.4$ has lower values (2.64–2.83 GPa). As a reference, pure Ti is 2.61 GPa, which is significantly higher than the pure Au (0.41 GPa). The pure Ti and Au samples measured were casted from the melt without any annealing. Further annealing on $Ti_{1-x}Au_x$ alloys resulted in insignificant changes in the hardness.

In group-I, the $Ti_{0.75}Au_{0.25}$ alloy ($x = 0.25$) has the highest hardness of 7.80 GPa, similar to high-carbon martensitic steels [16]. Fig. 2a is an SEM image of the as-cast sample. It shows a large area of primary matrix phase, with a very small fraction of secondary phase particles. Dislocations or stacking faults are not observed in the primary matrix phase by TEM diffraction contrast bright field (BF) imaging (see Fig. 2b). The primary phase was identified as β-Ti_3Au by HAADF-STEM

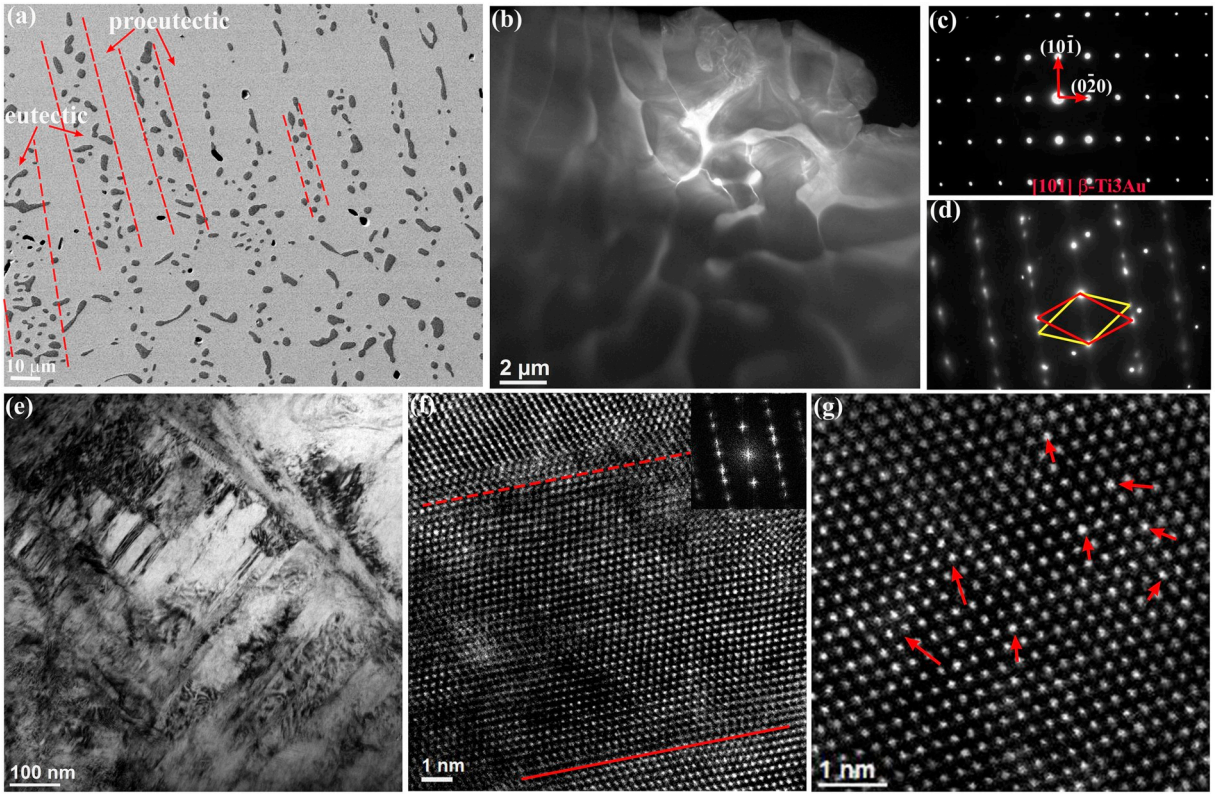

Fig. 3. (a) SEM image of $Ti_{0.78}Au_{0.22}$ with some of the eutectic region indicated between two dashed lines. (b) BF-TEM image of the eutectic region showing β-Ti_3Au with dark contrast and fcc Ti of the white contrast stripes. (c) Diffraction pattern of β-Ti_3Au along [101]. (d) Diffraction pattern of fcc Ti along [110]; the yellow and red frames indicate a twin relationship. (e) BF-TEM image of the fcc Ti of the eutectic region. (f) Atomic resolution HAADF-STEM *Z*-contrast image along [110] fcc Ti showing one nanotwin; inset: FFT pattern of this region confirming the twin structure. (g) Atomic resolution HAADF-STEM Z-contrast image along [110] fcc Ti showing the Ti columns containing Au atoms. (For interpretation of the references to color in this figure legend, the reader is referred to the web version of this article.)

z-contrast image (Fig.2c) and electron diffraction pattern (Fig. 2d). The secondary phase has an insignificantly small volume fraction, therefore is not included in the TEM study. It is likely α-Ti_3Au, as inferred from the X-ray diffraction data. Since $Ti_{0.75}Au_{0.25}$ alloy has only one dominating phase, so β-Ti_3Au is the hardest of all $Ti_{1-x}Au_x$ alloys.

With slightly lower Au composition at $x = 0.22$, for alloy $Ti_{0.78}Au_{0.22}$, the microstructure is changed as shown in Fig. 3. At this Au content, during the fast cooling, the β-Ti_3Au solidified largely as proeutectic dendritic branches as expected, shown in the SEM image as light grey contrast area in Fig. 3a. Fig. 3b is a BF-TEM image of the eutectic region at low magnification, corresponding to the co-existed two phase eutectic region between the dendrites in the SEM image. The "worm shaped" darker contrast are β-Ti_3Au, as confirmed by the selected area diffraction pattern shown in Fig. 3c, where the d-spacing is 3.60 ± 0.02 Å and 2.58 ± 0.02 Å, corresponding to {101} and {200} planes in the [101] zone axis of β-Ti_3Au. The width of the β-Ti_3Au "worm" is about 1–2 μm. The brighter area between the β-Ti_3Au is a Ti (Au) solid solution containing < 7 at.% Au as determined by energy dispersive X-ray spectroscopy (EDS) analysis. The Ti(Au) solid solution is identified as fcc-Ti from the selected area diffraction pattern (Fig. 3d). Its lattice parameter is measured to be 4.30 Å, consistent with the value reported in the literature [9]. With a width of only about 0.5 μm, the fcc-Ti region contains a high density of dislocations, stacking faults and nanotwins (Fig.3e–f). Since Au has a much higher atomic number than Ti, HAADF-STEM image is suitable to detect Au atoms dissolved in Ti matrix. Fig. 3g is the HAADF-STEM image of [110] Ti. The atomic columns with more substituted Au atoms show a brighter contrast as indicated by arrows. This image also suggests that Au atoms disperse randomly in Ti. The measured 7 at.% Au in Ti(Au) solid solution was far beyond the solubility of Au in α-Ti, which is < 1 at.% at room temperature, indicating a larger solute atom solubility in the fcc structure than the hcp structure. The combination of SEM and TEM results indicates that neither eutectic reaction nor eutectoid reaction described by the equilibrium phase diagram occurred in the region studied by TEM. It is likely that after β-Ti_3Au solidifies, some of the remaining liquid between dendrites forms the metastable fcc-Ti(Au). Although bulk Ti may be soft, the Ti(Au) phase here is constrained by the hard β-Ti_3Au and strengthened by the Au solute atoms. So overall this $Ti_{0.78}Au_{0.22}$ alloy is only slightly softer than $Ti_{0.75}Au_{0.25}$.

At a higher Au content of $x = 0.335$, the hardness of the $Ti_{0.665}Au_{0.335}$ alloy is decreased to 6.55 GPa, but still close to the hardest $Ti_{0.75}Au_{0.25}$ alloy, remaining in group-I. The phases present are identified as α-Ti_3Au, β-Ti_3Au and β-TiAu as evident by TEM (Fig. 4) and XRD data. The SEM image (Fig. 4a) shows a large region of the sample with two contrasted areas similar in volume fraction, a typical eutectic reaction product. The BF-TEM image (Fig. 4b) shows alternating black and white stripes with a width of about 200–300 nm from a similar region like the one with finer features in the SEM image.

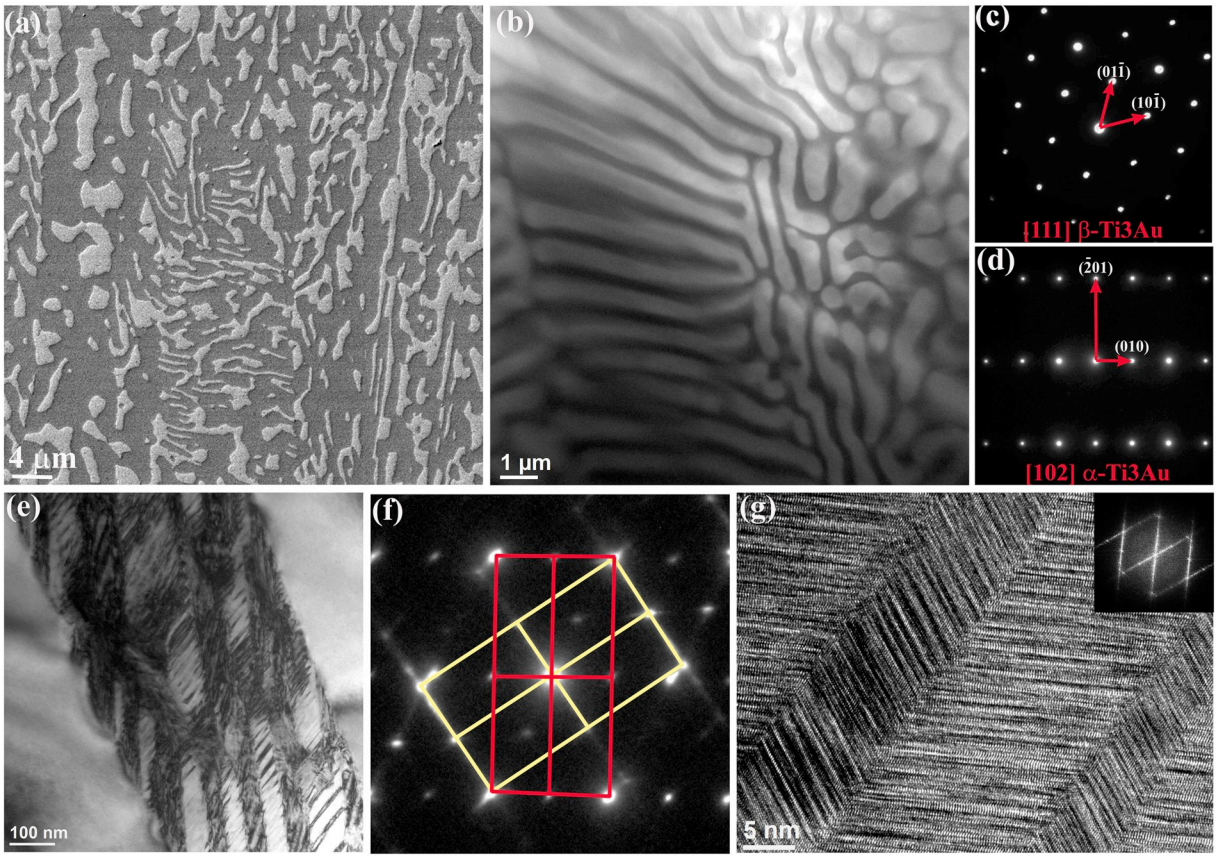

Fig. 4. (a) SEM image of $Ti_{0.665}Au_{0.335}$ showing a eutectic product of β-Ti_3Au (α-Ti_3Au) and β-TiAu. (b) BF-TEM image of the eutectic region (white contrast area: β-Ti_3Au or α-Ti_3Au; dark contrast stripes: β-TiAu. (c) Diffraction pattern from [111] β-Ti_3Au. (d) Diffraction pattern from [102] α-Ti_3Au. (e) BF-TEM image of β-TiAu showing high density twins. (f) Diffraction pattern of martensite β-TiAu. The yellow and red frames indicate the two sets of twins. (g) HRTEM image of martensite β-TiAu showing high density lines of planar defects; inset: FFT pattern. (For interpretation of the references to color in this figure legend, the reader is referred to the web version of this article.)

Selected area diffraction patterns confirmed the white background regions to be either α-Ti_3Au or β-Ti_3Au phases (Fig. 4c and d), which corresponds to the darker grey contrasted area in SEM image. Since β-Ti_3Au is the equilibrium phase from the phase diagram, and α-Ti_3Au is transformed from β-Ti_3Au induced by impurities [10], it is very likely that β-Ti_3Au has a higher volume fraction and only a small amount of α-Ti_3Au forms in this alloy. A closer look at the dark stripes reveals that they are the martensite β-TiAu B19-type structure (Fig. 4e and f). The corresponding diffraction pattern is indexed using two sets of [110] twins superimposed. Within the dark stripes, there is a high density of martensite β-TiAu nanotwins and they show lens or lath shapes with a width ranging between 10 and 130 nm. The twin-within-twin microstructure is typically observed in β-TiAu [14]. Within the individual martensite twin, an extremely high density of stacking faults or thin nanotwins is observed (Fig. 4g). The diffraction spots become streaks due to the high density planar defects, and the lines visible in the HRTEM image arise from the diffraction beam interference at the faults.

For $x = 0.5$, $Ti_{0.5}Au_{0.5}$ alloy in group-II, the major phase is β-TiAu, determined by selected area diffraction (Fig. 5a), where the d-spacings are 4.94 ± 0.02 Å and 2.92 ± 0.02 Å corresponding to {001} and {010}, respectively. Also in this compound, there is a high density of twins, stacking faults and dislocations in β-TiAu (Fig. 5b–d).

At $x = 0.6$, three distinct morphologies are observed as shown in Fig. 6a: a lens-shaped martensite region that is labeled as R1 (a close-up in Fig. 6b), a checkerboard region labeled as R2 (a close-up in Fig. 6c), and a perfect region without defects that is labeled as R3. The diffraction pattern from R1 has d-spacings of 2.39 ± 0.02 Å, 2.17 ± 0.02 Å and 1.20 ± 0.02 Å, consistent with $TiAu_2$ [331] zone axis diffraction pattern (Fig. 6d). The perfect defect-free R3 area has d-spacing of 4.04 ± 0.02 Å, and 2.91 ± 0.02 Å, corresponding to α-Ti_3Au [101] zone axis diffraction pattern (Fig. 6e). The diffraction pattern from R2 has strong streaks indicating a high density of planar defects (Fig. 6f). The phase of the checkerboard region R2 is found to be fcc Au, as described in detail in Fig. 7. The R2 and R3 regions are sandwiched between the R1 regions. We believe that $TiAu_2$ (R1) crystallizes first from the melt, leaving the eutectic solution to later cool into non-equilibrium phases of α-Ti_3Au (R3) and fcc Au(Ti) (R2) solid solution.

Fig. 7 presents the details of the microstructure and phase identification of the checkerboard region R2 of the $Ti_{0.4}Au_{0.6}$ alloy. The general morphology of this phase is shown in a BF-TEM image (Fig. 7a), which reveals a checkerboard pattern formed by two sets of white and dark stripes of about 10 nm width, crisscrossing at a right angle. This unique microstructure is similar to the morphology of an unidentified microstructure with composition $Ti_{0.5}Au_{0.5}$ reported earlier [17]. Upon

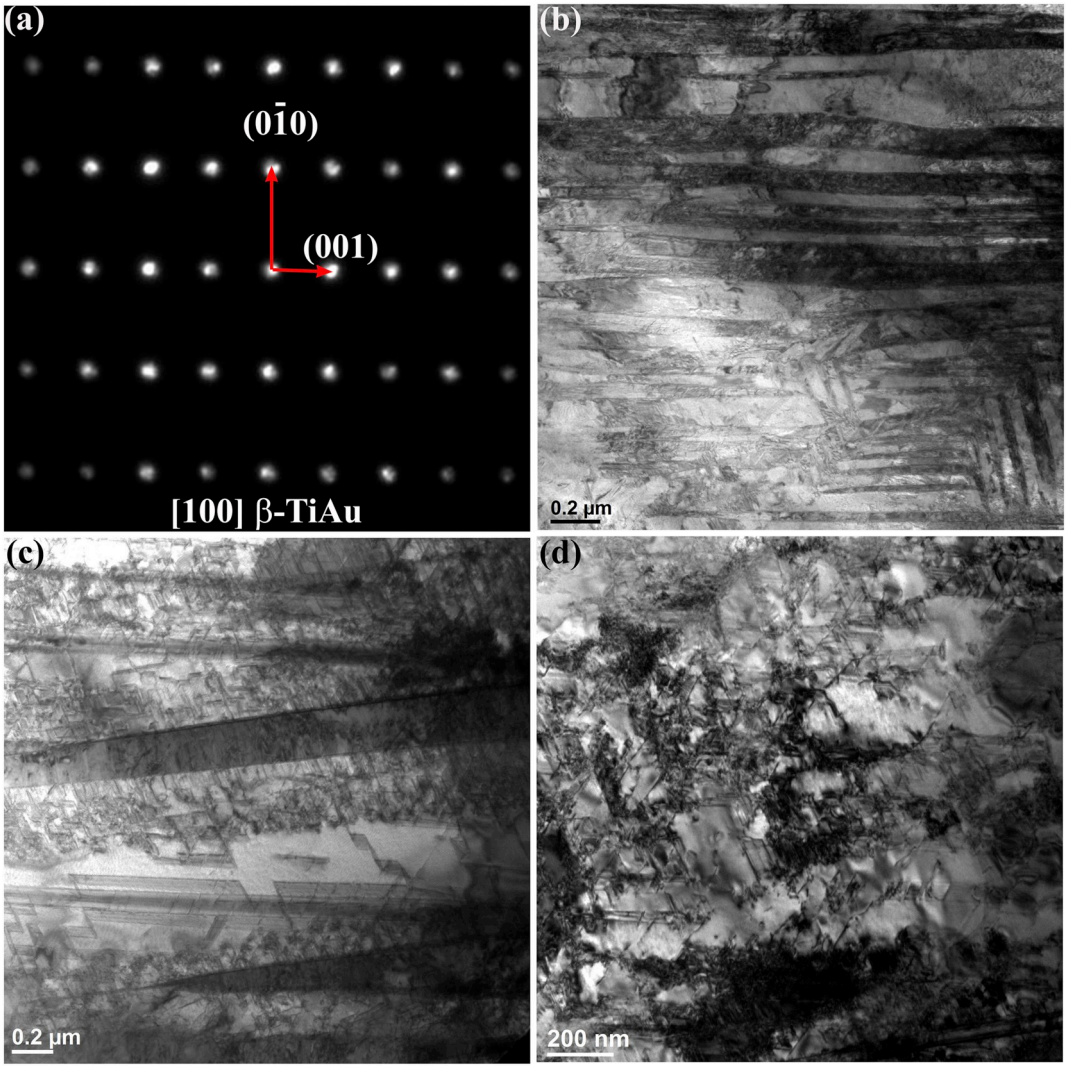

Fig. 5. (a) Diffraction pattern of [100] β-TiAu. (b)–(d) BF-TEM images of β-TiAu showing twins and dislocations.

further magnification, the features show up clearly in the HRTEM image (Fig. 7b). Each dark and white stripe in fact contains high density planar defects. For the adjacent stripes, the defects in the dark stripe are perpendicular to the defects in the adjacent white stripe. The fast Fourier transform (FFT) shows continuous streaks that are consistent with the high density planar defects in the structure (Fig. 7c). The atomic structures of these defects are revealed in the HAADF-STEM image (Fig. 7d and e). The atomic columns show similar, bright intensities, indicating either Au/Ti or Au columns. The d-spacing measured for the atomic plane indicated by straight lines is 2.35 ± 0.02 Å, corresponding to {111} Au. EDS from this region gives a composition of about 18 at.% Ti and 82 at.% Au. The atoms in HAADF-STEM image correspond to the projected crystal structure and together with the diffraction patterns or FFTs (Fig. 7f–h), it is determined that this phase is fcc Au with Ti substitution, i.e. a Au(Ti) solid solution. The Ti solubility in Au is up to 12 at.% [6], therefore, the detected Ti composition is within the expected error. The dark patches imply additional segregation of Ti into these Au atomic columns, indicating that Ti is not uniformly dispersed in Au. Fig. 7d and e are lattice images of Au crystals along ⟨110⟩, and the high density planar defects are clearly revealed. These defects are continuous thin {111} nanotwins with width of only 2 or 3 {111} atomic planes, as indicated by the curvy line that consists of small straight segments, where one straight line segment indicates one nanotwin. A typical twin structure in fcc crystal has a stacking sequence of …*ABCAB*<u>*CAC*</u>*BACB*…, where the <u>*CAC*</u> stacking is at the coherent twin boundary. We have found that it is quite common that these nanotwins form an ordered stacking sequence, such as those indicated by the red line in Fig. 7d. The stacking sequence is *AB*<u>*CAC*</u>*B*<u>*CAC*</u>*B*<u>*CAC*</u>*B*<u>*CAC*</u>*B*<u>*CAC*</u>*BAB*<u>*CAC*</u>*BABC*…, where the nanotwins just separated by one *B* layer. This ordered stacking has a repeat unit of 4 atomic layer *CACB*, which is reflected in its FFT diffraction pattern where the diffractions become discrete spots and there are 4 diffraction spots in between the major diffraction (Fig. 7d inset). The bright and dark areas in the diffraction contrast BF image in Fig. 7a are crystals that are rotated 90° with respect to each other, with their {111} atomic planes meeting at the boundary that is on the (001) plane (see Fig. 7e). These boundaries are wavy as clearly revealed in Fig. 7b. The diffraction pattern or FFT pattern from the checkerboard region can be

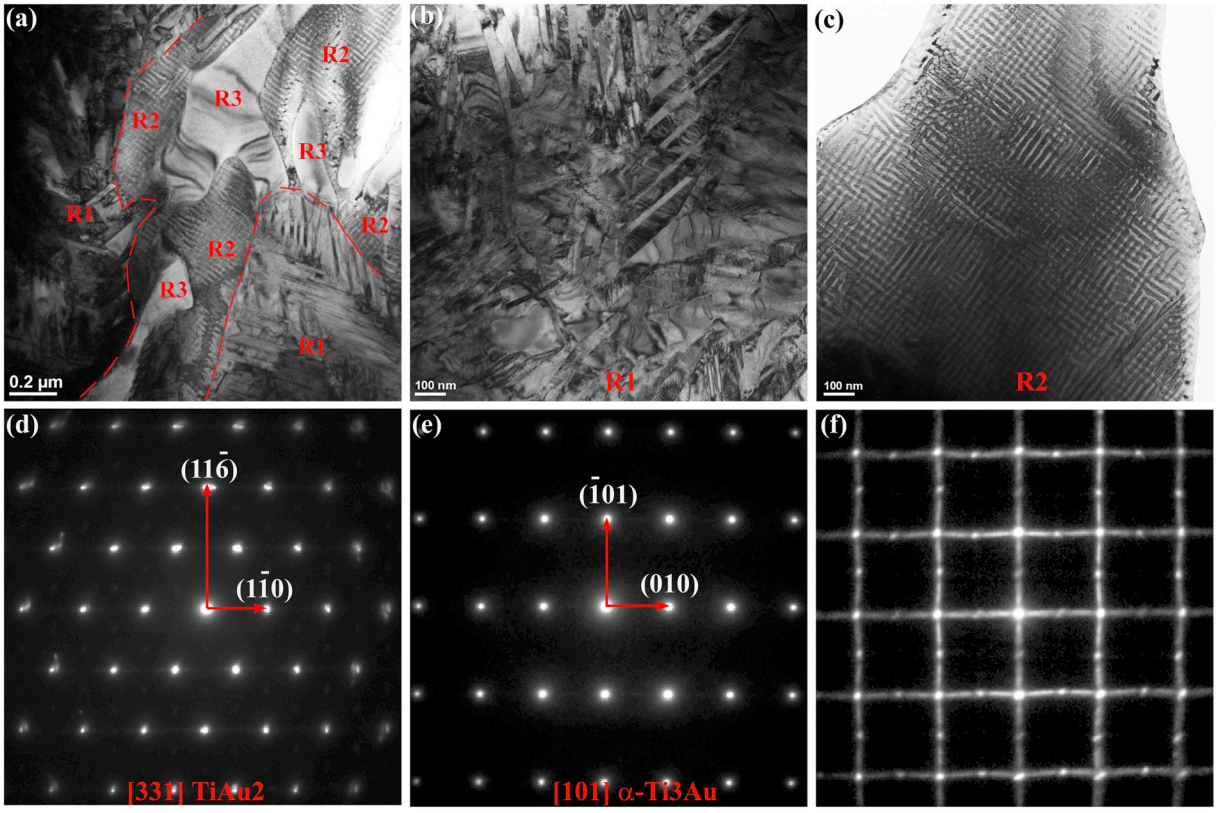

Fig. 6. (a) BF-TEM image of $Ti_{0.4}Au_{0.6}$ alloy. R1: $TiAu_2$; R2: Au; R3: α-Ti_3Au. (b) BF-TEM image of R1 ($TiAu_2$) showing lens-shaped martensites. (c) BF-TEM image of R2 (Au) showing the checkerboard pattern. (d) Diffraction pattern from [331] $TiAu_2$. (e) Diffraction pattern from [101] α-Ti_3Au. (f) Diffraction pattern from R2 (Au).

reproduced by two superimposed [110] diffraction patterns that are rotated by 90° from each other, as illustrated in Fig. 7i.

At $x = 0.8$, for the Au rich alloy $Ti_{0.2}Au_{0.8}$, the detailed microstructure is shown in Figs. 8 and 9. There are two types of crystal grain morphologies formed: large grain areas (labeled as A1) and smaller grains in between (labeled as A2), as illustrated in Fig. 8a. The defects observed in the large grains are dislocation networks (Fig. 8b) and microtwins (Fig. 8c). Three phases are identified from selected area diffraction patterns: $TiAu_4$, γ-$TiAu_2$ and fcc Au (Fig. 8d–f). In Fig. 8d, the measured d-spacing for the stronger reflections is 2.04 ± 0.02 Å, corresponding to the {310} planes of $TiAu_4$. The weaker reflections with d-spacings of 4.53 ± 0.02 Å and 3.21 ± 0.02 Å correspond to {110} and {020} planes of $TiAu_4$, and it is the [001] zone axis of $TiAu_4$. The measured d-spacings for Fig. 8e are 2.21 ± 0.02 Å, 1.69 ± 0.02 Å and 1.33 ± 0.02 Å, which are consistent with $TiAu_2$ [301] zone axis. Its atomic resolution HAADF-STEM image is shown in Fig. 8g, where each atomic column contains one Ti atom for every two Au atoms along this direction. In Fig.8f, the d-spacing of the strong reflections is 1.44 ± 0.02 Å, with an angle of 60° between the diffraction spots, which corresponds to Au {220} of the [111] zone axis. Fig. 8h shows the HAADF-STEM image of [111] Au from the large grain area. It shows the typical Au [111] projection of atomic columns, with the exception of some darker contrast columns, interspersing the image with darker patches and speckles. The line intensity profiles in Fig. 8i and j confirm the existence of lower intensity columns compared to the surrounding ones. If Ti atoms were uniformly distributed throughout the Au lattice, the Au atomic columns are expected to have similar intensities. Therefore the intensity variations indicate that dissolved Ti atoms are in somewhat ordered positions, forming nano-scale clusters. This is further confirmed by the diffuse, weak spots in the diffraction pattern shown in Fig. 8f, marked by small arrows. These reflections have a d-spacing of 2.48 ± 0.02 Å and an angle of 60°, close to the {110} planes of γ-TiAu, but with a significantly larger lattice parameter of 3.51 Å compared to the lattice parameter of 3.25 Å for γ-TiAu. Therefore, γ-TiAu crystals have not matured but remain in highly strained nanometer-sized clusters embedded in the Au lattice.

The detailed microstructure of the small grained area of the $Ti_{0.2}Au_{0.8}$ alloy is shown in Fig. 9. The morphology of this area consists of crisscrossed long grains of 50–80 nm in width (Fig. 9a). Two phases are identified: ordered $TiAu_4$ and Au with minor amounts of Ti. Some of the grains show distinct super-lattice diffraction reflections (Fig. 9b), typical of [001] $TiAu_4$. Along this projection, the ordered Ti columns are on {110} planes separated by four Au column planes (Fig. 9d). This ordered feature is more pronounced in the inverse FFT image derived from these super-lattice diffraction spots, as shown in Fig. 9e. Other grains do not show super-lattice diffraction spots (Fig. 9c), and the HAADF-STEM image does not exhibit ordered intensity features (Fig. 9f). These grains are likely [001] fcc (Au,Ti) with Ti atoms randomly dissolved in the Au lattices.

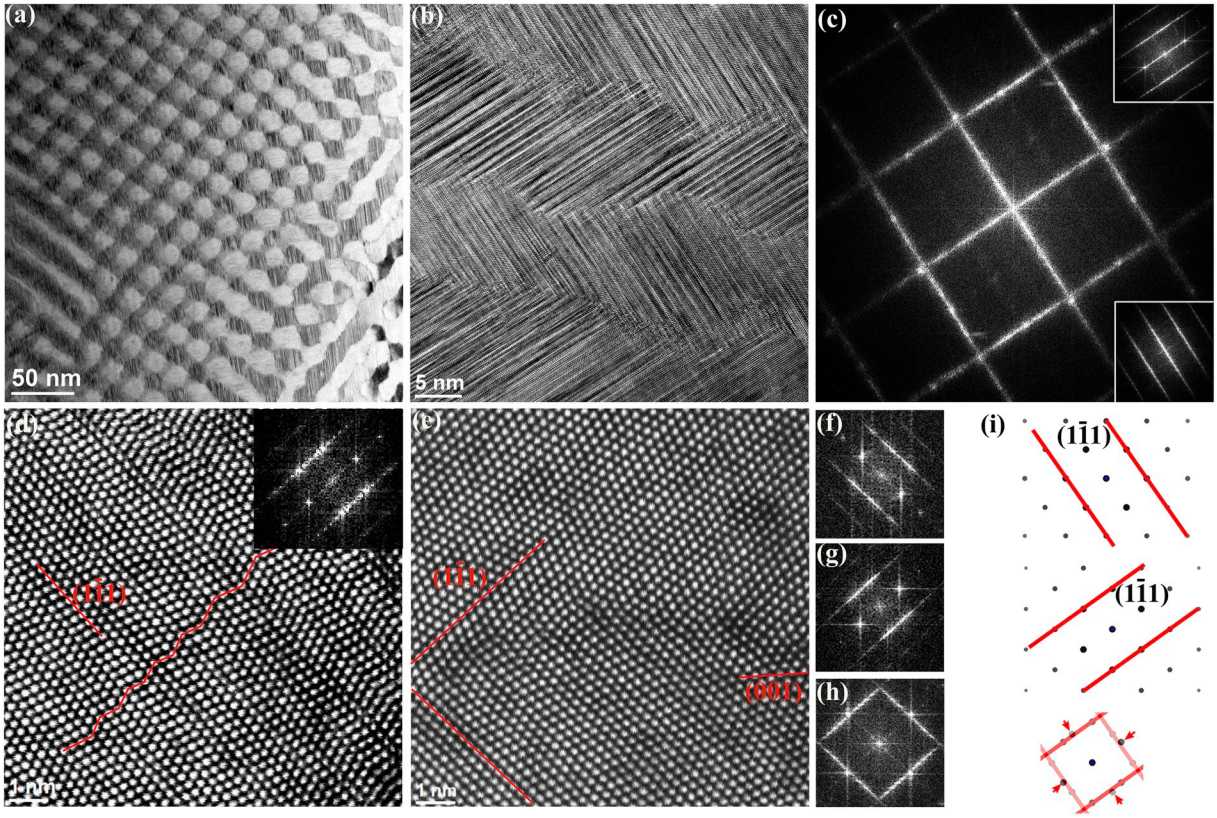

Fig. 7. (a) BF-TEM image of checkerboard area of $Ti_{0.4}Au_{0.6}$ alloy. (b) HRTEM image of white and dark stripes. (c) FFT pattern from (b). Upper inset: FFT from one tripe; lower inset: FFT from adjacent stripe. (d) Atomic resolution HAADF-STEM Z-contrast image of one stripe in Au (R2) along [110]. The nanotwins are indicated by red line. Inset: FFT pattern from this region. (e) Atomic resolution HAADF-STEM Z-contrast image of two stripes in Au (R2) along [110] showing the interface. (f) FFT pattern of the upper stripe in (e). (g) FFT pattern of the lower stripe in (e). (h) FFT pattern of both stripes in (e). (i) Simulated Au [110] diffraction patterns; the red lines indicate the diffraction streaks due to high density nanotwins. Upper pattern: one simulated Au [110] diffraction pattern; middle: the same pattern rotated 90° clockwise; lower: two superimposed 90° rotated pattern. This reproduced the FFT pattern in (h). (For interpretation of the references to color in this figure legend, the reader is referred to the web version of this article.)

4. Discussions

The hardness of the $Ti_{1-x}Au_x$ binary alloys are primarily governed by the constitutional intermetallic compounds and their microstructure created during fabrication. It is observed that casting of small ingots can produce significant volume fraction of metastable phases, and phases that form but do not follow the equilibrium phase diagram.

From experimental data, it is found that the harder alloys are in group-I and β-Ti_3Au is the major phase for each alloy in this group. It is known that atomic bond density and bond lengths are among the determining factors for the material hardness [18]. β-Ti_3Au has the highest bond density among $Ti_{1-x}Au_x$ alloys and α-Ti_3Au has a very similar but slightly smaller value, while all other phases such as TiAu, $TiAu_2$, and $TiAu_4$ have much smaller bond density [13]. So the crystal structure or the nature of atomic bonds of β-Ti_3Au leads to its high hardness. In addition, there are almost no defects observed in the β-Ti_3Au grains, in contrast to other $Ti_{1-x}Au_x$ phases. This indicates that β-Ti_3Au has almost no mobile defects and is brittle in nature. For $Ti_{0.78}Au_{0.22}$, the majority phase is still β-Ti_3Au, but in the form of wide dendrites, interspersed with fine dendrites of fcc Ti. Metallic materials hardening can usually be achieved by introducing defects, reducing grain sizes or having solute atoms, which all act as barriers for dislocation movement. The high density of defects and thin spacing of fcc Ti, in addition to the Au atoms in the Ti lattice, helped to harden the fine dendrites of fcc Ti. Therefore the hardness of $Ti_{0.78}Au_{0.22}$ is still high and only 8.9% lower than that of β-Ti_3Au. With an increased Au content, as in $Ti_{0.665}Au_{0.335}$, the dendrites of β-Ti_3Au become finer with an increased volume fraction of β-TiAu martensite. The highly defected β-TiAu martensite is not as hard as β-Ti_3Au, but due to its high density nanotwins, the alloy hardness value reduced only by about 16.0%. Group-I sample annealing does not soften them significantly, which is consistent with the fact that the high hardness is intrinsic to the crystal structure of the dominant phase β-Ti_3Au. Moreover, it is hard for the defects in minority phases such as fcc Ti to move due to the small size of fcc Ti grains that are bordered by β-Ti_3Au.

Alloys with 50 at.% Au or more no longer form β-Ti_3Au, and their hardness decreases significantly, similar to that of pure Ti metal but much higher than that of pure Au. We believe, this is due to high density dislocations and planar defects such as twinned martensites, and high density narrow nanotwins. The refined nanotwins and martensites provide an extra hardening mechanism in the materials. Annealing $Ti_{0.5}Au_{0.5}$ reduced the hardness only by about 11%. It is speculated that the martensitic twins and nanotwins did not annihilate due to the restrains imposed by their high density. While for $Ti_{0.4}Au_{0.6}$ alloy, annealing causes the dislocation and twin density to reduce significantly due to its low density and larger grain size, resulting in the largest hardness drop of all alloys.

The two most interesting findings in this work are the hard defect-free β-Ti_3Au intermetallic and nanotwin-microstructured Au, as both have high hardness due to the crystal structure or the interlocked 3D high density nanotwins respectively. High density nanotwins can also be realized in fcc structure such as in Cu by pulsed electrodeposition [19]. High hardness is usually associated with good wear resistance. Hard coatings are thin films that are deposited on tool substrates in order to improve their properties [20]. We speculate that β-Ti_3Au or nanotwinned Au thin films could be achieved through electrodeposition

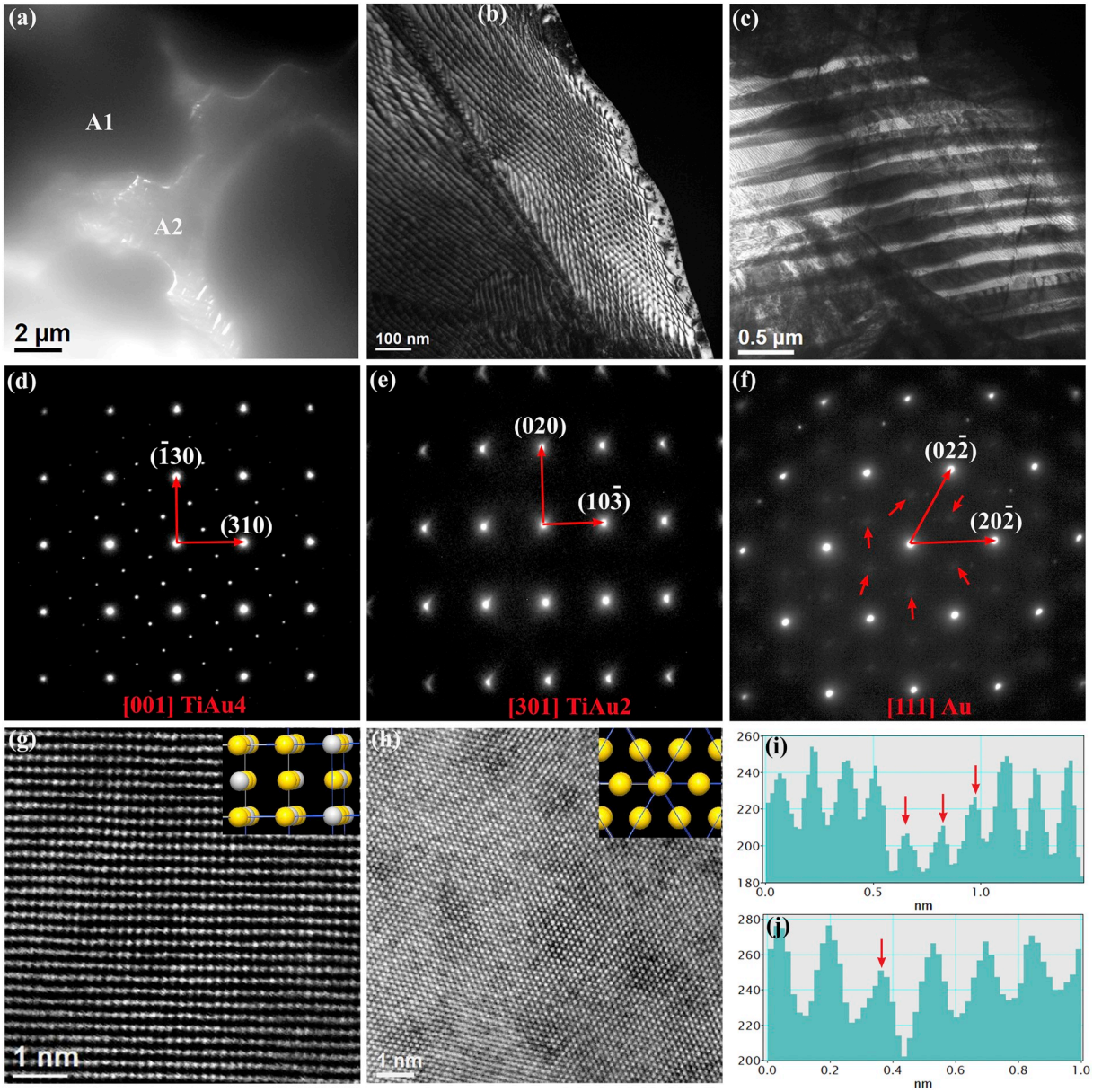

Fig. 8. (a) Low magnification BF-TEM image of alloy $Ti_{0.2}Au_{0.8}$. (b) Dark field TEM image showing dislocation networks from big grain region. (c) BF-TEM image of twins from big grain region. (d) Diffraction pattern of [001] $TiAu_4$. (e) Diffraction pattern of [301] $TiAu_2$. (f) Diffraction pattern of [111] Au. (g) Atomic resolution HAADF-STEM Z-contrast image of [301] $TiAu_2$. (h) Atomic resolution HAADF-STEM Z-contrast image of [111] Au. (i)–(j) Intensity line profiles of Au atom columns from (h). The lower intensity columns are indicated by re arrows.

for many bio-compatible applications, such as a possible dental restorative coating or hip joints coating.

5. Conclusions

The detailed microstructures of the various Ti—Au phases formed when quenching $Ti_{1-x}Au_x$ alloys (x = 0.22–0.8) from the melt were studied by TEM. The hardness of these alloys are measured and can be divided into two groups: group-I has higher hardness of about 6.55–7.80 GPa; group-II alloys are softer with hardness of 2.64–2.83 GPa, which is similar to that of pure cast Ti (2.61 GPa). In group-I, β-Ti_3Au is the hardest alloy. Other alloys in this group with a significant amount of β-Ti_3Au also have relatively high hardness. Although brittleness of β-Ti_3Au is likely to render it less suitable for dental applications in bulk form, the hard coating of β-Ti_3Au should find valuable applications. In group-II, for $Ti_{1-x}Au_x$ alloys with $x \geq 0.5$, the lack of β-Ti_3Au is the main reason why they are significantly softer. However, high density of defects such as nanotwins renders them to be as hard as pure Ti, much harder than pure Au. An unequilibrium fcc Ti phase was found in $Ti_{0.78}Au_{0.22}$. A previously unidentified microstructure with checkerboard contrast is determined to be an Au(Ti) fcc solid solution with an extremely high density of nanotwins of 2 to 3 atomic layers thick that intertwine in three dimension. It is noted from this study that the material's hardness is decided mainly by the crystal structure and atomic bonding of its dominating phase and an incremental hardness improvement could be achieved through introducing high density of defects.

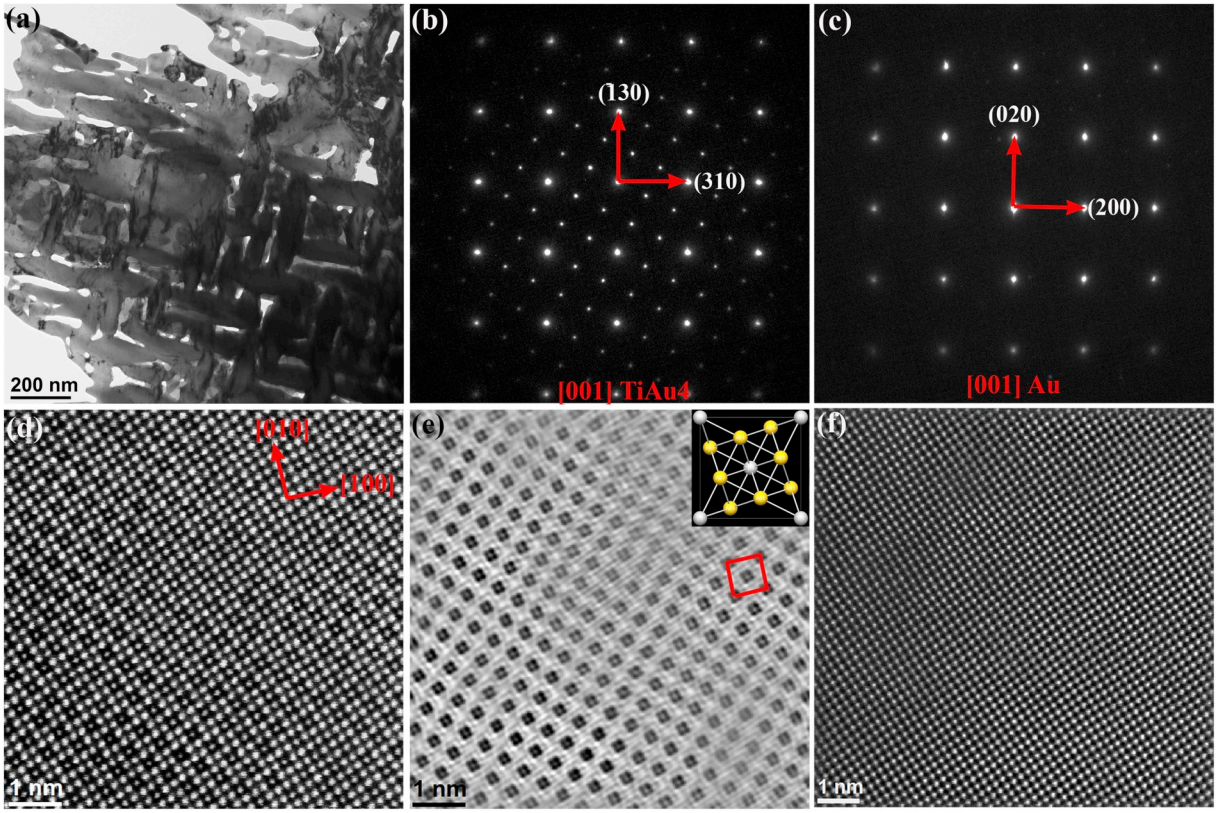

Fig. 9. (a) BF-TEM image of the small grain area in alloy $Ti_{0.2}Au_{0.8}$. (b) Diffraction pattern of [001] $TiAu_4$. (c) Diffraction pattern of [001] Au. (d) Atomic resolution HAADF-STEM Z-contrast image of [001] $TiAu_4$. (e) Inverse FFT image of [001] $TiAu_4$ using superlattice spots. (f) Atomic resolution HAADF-STEM Z-contrast image of [001] Au.

Acknowledgment

This work was performed at the National High Magnetic Field Laboratory of Florida State University, which is supported by National Science Foundation Cooperative Agreement Nos. DMR-1157490 and DMR-1644779, and the State of Florida. EM and TS acknowledge funding from NSF DMR-1506704.

Data Availability

The raw data required to reproduce these findings are available to download from https://nationalmaglab.org. The processed data required to reproduce these findings are available to download from https://nationalmaglab.org.

References

[1] J. Fischer, J. Biomed. Mater. Res. 52 (2000) 678–686.
[2] M. Long, H.J. Rack, Biomaterials 19 (1998) 1621–1639.
[3] M. Takahasgi, M. Kikuchi, O. Okuno, Dent. Mater. J. 23 (2004) 203–210.
[4] Yong-Ryeol Lee, Mi-Kyung Han, Min-Kang Kim, Won-Jin Moon, Ho-Jun Song, Yeong-Joon Park, Gold Bull. 47 (2014) 153–160.
[5] Keyoung Jin Chun, Jong Yeop Lee, J. Dent. Biomech. 5 (2014) 1–6.
[6] J.L. Murray, Bull. Alloy Phase Diagr. 4 (1983) 278–283.
[7] W. Luo, Z. Jin, H. Liu, T. Wang, Calphad 25 (2001) 19–26.
[8] Qian Yu, Josh Kacher, Christoph Gammer, Rachel Traylor, Amit Samanta, Zhenzhong Yang, Andrew M. Minor, Scr. Mater. 140 (2017) 9–12.
[9] G. Han, X. Lu, Q. Xia, B. Lei, Y. Yan, C.J. Shang, J. Alloys Compd. 748 (2018) 943–952.
[10] H. von Philipsborn, F. Laves, Acta Cryst 17 (1964) 213–214.
[11] H.C. Donkersloot, J.H.N. Van Vucht, J. Less Common Metals 20 (1970) 83–91.
[12] H. Hosoda, R. Tachi, T. Inamura, K. Wakashima, S. Miyazaki, Mater. Sci. Forum 561-565 (2007) 1541–1544.
[13] E. Svanidze, T. Besara, M.F. Ozaydin, C.S. Tiwary, J.K. Wang, S. Radhakrishnan, S. Mani, Y. Xin, K. Han, H. Liang, T. Siegrist, P.M. Ajayan, E. Morosan, Sci. Adv. 2 (2016) 1600319.T.
[14] Inamura, H. Hosoda, Metall. Mater. Trans. A 42 (2011) 111–120.
[15] P. Zhang, S.X. Li, Z.F. Zhang, Mater. Sci. Eng. A 529 (2011) 62–73.
[16] L. Cui, H. Fujii, N. Tsuji, K. Nogi, Friction stir welding of a high carbon steel, Scr. Mater. 56 (2007) 637–640.
[17] S.K. Wu, C.M. Wayman, Metallography 20 (1987) 359–376.
[18] Faming Gao, Julong He, Erdong Wu, Shimin Liu, Dongli Yu, Dongchun Li, Siyuan Zhang, Yongjun Tian, Phys. Rev. Lett. 91 (2003) 015502.
[19] R.M. Niu, K. Han, Y.F. Su, T. Besara, T.M. Siegrist, X.W. Zuo, Nat. Sci. Rep. 6 (2016) 31410.
[20] D. Cameron, Films and coatings: technology and recent development, in: Saleem Hashmi, Chester J. Van Tyne, Gilmar Ferreira Batalha, Bekir Yilbas (Eds.), Comprehensive Materials Processing, Elsevier Ltd., 2014, pp. 1–561.